

# Histogram-free reweighting to estimate vapor-liquid coexistence properties of non-simulated force fields

Richard A. Messerly,<sup>\*,†</sup> Mohammad S. Barhaghi,<sup>‡</sup> Jeffrey J. Potoff,<sup>‡</sup> and  
Michael R. Shirts<sup>¶</sup>

<sup>†</sup>*Thermodynamics Research Center, National Institute of Standards and Technology, Boulder,  
Colorado, 80305, United States*

<sup>‡</sup>*Department of Chemical Engineering and Materials Science, Wayne State University, Detroit,  
Michigan 48202, United States*

<sup>¶</sup>*Department of Chemical and Biological Engineering, University of Colorado, Boulder,  
Colorado, 80309, United States*

E-mail: richard.messerly@nist.gov

---

Contribution of NIST, an agency of the United States government; not subject to copyright in the United States.

# Abstract

## 1 Introduction

A key use of molecular simulation is the ability to accurately and efficiently estimate vapor-liquid coexistence properties, i.e., saturated liquid density ( $\rho_{\text{liq}}^{\text{sat}}$ ), saturated vapor density ( $\rho_{\text{vap}}^{\text{sat}}$ ), saturated vapor pressures ( $P_{\text{vap}}^{\text{sat}}$ ), and enthalpy of vaporization ( $\Delta H_v$ ). The accuracy of coexistence estimates depends on the underlying molecular model (a.k.a., force field, potential model, or Hamiltonian) while the computational efficiency depends primarily on the simulation methods, software, and hardware.

Several simulation approaches exist for computing vapor-liquid coexistence properties.<sup>1</sup> These include Gibbs Ensemble Monte Carlo (GEMC), two-phase molecular dynamics (2 $\phi$ MD),<sup>2</sup> isothermal-isochoric integration (ITIC),<sup>3</sup> and Grand Canonical Monte Carlo coupled with histogram reweighting (GCMC-HR). Although the development of accurate force fields has been greatly enabled by the improved efficiency of these methods, parameterization of non-bonded interactions with vapor-liquid coexistence calculations over a wide range of temperatures remains an arduous and time-consuming task.<sup>4-8</sup>

The primary objective of this study is to reduce the computational cost of optimizing non-bonded parameters with vapor-liquid saturation properties. This is achieved by substituting histogram reweighting with the Multistate Bennett Acceptance Ratio (MBAR),<sup>9,10</sup> a histogram-free reweighting schema. The proposed GCMC-MBAR method is identical to the traditional GCMC-HR approach except that it uses MBAR to reweight configurations rather than reweighting histograms. The benefit of this simple modification is that GCMC-MBAR can estimate coexistence properties for non-bonded parameter sets that have not been simulated directly.

In similar studies, Messerly et al. demonstrate how to combine MBAR with ITIC

(MBAR-ITIC) to optimize generalized Lennard-Jones (Mie  $\lambda$ -6) potentials.<sup>11,12</sup> For MBAR-ITIC, a series of  $NVT$  simulations along an isotherm and isochore(s) are performed with a “reference” force field(s) ( $\theta_{\text{ref}}$ ). MBAR reweights configurations sampled with  $\theta_{\text{ref}}$  to estimate the internal energy ( $U$ ) and pressure ( $P$ ) at each  $T, \rho$  state point for a non-simulated (“rerun”) force field ( $\theta_{\text{rr}}$ ). ITIC then converts the  $U$  and  $P$  estimates into vapor-liquid coexistence properties.<sup>3,13</sup>

The results from Messerly et al. demonstrate that MBAR-ITIC is most reliable in the local domain, i.e., when  $\theta_{\text{rr}} \approx \theta_{\text{ref}}$ .<sup>11</sup> Furthermore, MBAR-ITIC performs best for changes in the non-bonded well-depth parameter ( $\epsilon$ ) while it performs significantly worse for large changes in the non-bonded size and repulsive parameters ( $\sigma$  and  $\lambda$ , respectively). This is typically referred to as poor “overlap” and can be quantified by the “number of effective snapshots” ( $K_{\text{snaps}}^{\text{eff}}$ ), which is essentially the number of non-negligible samples that contribute to the estimated ensemble averages. Poor overlap (low  $K_{\text{snaps}}^{\text{eff}}$ ) is especially problematic for MBAR-ITIC as a large number of snapshots is needed to obtain precise estimates of  $P$  in the liquid phase, due to large fluctuations in  $P$  at high densities.

Our initial hypothesis was that GCMC-MBAR should experience better overlap than what was observed for MBAR-ITIC when  $\theta_{\text{rr}} \not\approx \theta_{\text{ref}}$ . There were two main reasons for this hypothesis/aspiration. First, as opposed to the fixed density  $NVT$  simulations used in ITIC, the fluctuating density in GCMC simulations produces a wider range of configurations and energies. Second, ITIC requires larger box sizes (and, thereby, more molecules) than those typically utilized with GCMC. By utilizing fewer molecules, GCMC simulations experience larger energy fluctuations (on a percent basis) which improves the overlap between states. We also hypothesized that the impact of poor overlap would be less severe compared to MBAR-ITIC, where poor overlap leads to sporadic values of  $P$  and nonsensical coexistence estimates.

The method outlined in this study is similar in spirit to “Hamiltonian scaling” (HS),

which has been applied to both GEMC<sup>14</sup> and GCMC simulations.<sup>1,15–17</sup> The HS approach samples from multiple force fields (Hamiltonians) in a single simulation according to a weighted sampling probability. Vapor-liquid coexistence curves for each force field are estimated post-simulation by reweighting the configurations accordingly. For the Grand Canonical Monte Carlo implementation of Hamiltonian scaling (HS-GCMC),  $\mu$  and  $T$  are not stationary during the simulation, rather the current value of  $\mu$  and  $T$  depends on which force field is being sampled. Despite HS-GCMC proving to be a powerful tool to optimize force field parameters,<sup>1,15–17</sup> it has yet to gain widespread popularity. This is likely due to the added complexity of both the simulation protocol and the histogram post-processing. Also, HS requires that a decision be made *a priori* regarding which force fields are to be tested. By contrast, GCMC-MBAR does not require any modification of the simulation procedure, the post-processing is essentially unchanged, and the non-bonded parameter sets need not be selected prior to the simulations.

The outline for this study is the following. Section 2 provides details regarding the force fields, simulation set-up, and post-simulation analysis with MBAR. Section 3 provides a comparison of GCMC-MBAR and GCMC-HR as well as various applications of GCMC-MBAR for force field parameterization. Section 4 discusses some limitations and provides recommendations for future work. Section 5 presents the primary conclusions.

## 2 Methods

### 2.1 Force fields

The force fields utilized in this study are Transferable Potentials for Phase Equilibria (TraPPE-UA, also referred to simply as TraPPE<sup>4,18,19</sup>), Mie Potentials for Phase Equilibria (MiPPE),<sup>6,20</sup> and Nath, Escobedo, and de Pablo revised (NERD). Each force field adopts a

united-atom (UA) representation, where non-polar hydrogens are not modeled explicitly.

The bond lengths for the TraPPE, MiPPE, and NERD force fields are 0.154 nm for all compounds studied. The same angle and dihedral potentials are used for each force field, with the exception of the NERD  $\text{CH}_i\text{-CH-CH}_j$  equilibrium bond angle. Angular bending interactions are evaluated using a harmonic potential:

$$u^{\text{bend}} = \frac{k_\theta}{2} (\theta - \theta_0)^2 \quad (1)$$

where  $u^{\text{bend}}$  is the bending energy,  $\theta$  is the instantaneous bond angle,  $\theta_0$  is the equilibrium bond angle (see Table 1), and  $k_\theta$  is the harmonic force constant with  $k_\theta/k_B = 62500 \text{ K/rad}^2$  for all bonding angles, where  $k_B$  is the Boltzmann constant.

Table 1: Equilibrium bond angles ( $\theta_0$ ).<sup>18</sup>  $\text{CH}_i$  and  $\text{CH}_j$  represent  $\text{CH}_3$ ,  $\text{CH}_2$ ,  $\text{CH}$ , or  $\text{C}$  sites.

Bending sites	$\theta_0$ (degrees)
$\text{CH}_i\text{-CH}_2\text{-CH}_j$	114.0
$\text{CH}_i\text{-CH-CH}_j$	112.0
$\text{CH}_i\text{-CH-CH}_j$ , NERD	109.5
$\text{CH}_i\text{-C-CH}_j$	109.5

Dihedral torsional interactions are determined using a cosine series:

$$u^{\text{tors}} = c_0 + c_1[1 + \cos \phi] + c_2[1 - \cos 2\phi] + c_3[1 + \cos 3\phi] \quad (2)$$

where  $u^{\text{tors}}$  is the torsional energy,  $\phi$  is the dihedral angle and  $c_n$  are the Fourier constants listed in Table 2.

Non-bonded interactions between sites located in two different molecules or separated by more than three bonds within the same molecule are calculated using a Mie  $\lambda$ -6

Table 2: Fourier constants ( $c_n/k_B$ ) in units of K.<sup>18</sup>  $\text{CH}_i$  and  $\text{CH}_j$  represent  $\text{CH}_3$ ,  $\text{CH}_2$ ,  $\text{CH}$ , or C sites.

Torsion sites	$c_0/k_B$	$c_1/k_B$	$c_2/k_B$	$c_3/k_B$
$\text{CH}_i\text{-CH}_2\text{-CH}_2\text{-CH}_j$	0.0	355.03	-68.19	791.32
$\text{CH}_i\text{-CH}_2\text{-CH-CH}_j$	-251.06	428.73	-111.85	441.27
$\text{CH}_i\text{-CH}_2\text{-C-CH}_j$	0.0	0.0	0.0	461.29
$\text{CH}_i\text{-CH-CH-CH}_j$	-251.06	428.73	-111.85	441.27

potential (of which the Lennard-Jones, LJ, 12-6 is a subclass):

$$u^{\text{nb}}(\epsilon, \sigma, \lambda; r) = \left( \frac{\lambda}{\lambda - 6} \right) \left( \frac{\lambda}{6} \right)^{\frac{6}{\lambda - 6}} \epsilon \left[ \left( \frac{\sigma}{r} \right)^\lambda - \left( \frac{\sigma}{r} \right)^6 \right] \quad (3)$$

where  $u^{\text{nb}}$  is the non-bonded energy,  $\sigma$  is the distance ( $r$ ) where  $u^{\text{nb}} = 0$ ,  $-\epsilon$  is the energy of the potential at the minimum (i.e.,  $u^{\text{nb}} = -\epsilon$  and  $\frac{\partial u^{\text{nb}}}{\partial r} = 0$  for  $r = r_{\text{min}}$ ), and  $\lambda$  is the repulsive exponent.

The non-bonded Mie  $\lambda$ -6 force field parameters for TraPPE, MiPPE, and NERD are provided in Table 3. MiPPE reports a “generalized” (MiPPE-gen) and “short/long” (MiPPE-SL) CH and C parameter set. The “short” and “long” parameters are implemented when the number of carbons in the backbone is  $\leq 4$  and  $> 4$ , respectively. Also note that the NERD force field has several different parameter sets for  $\text{CH}_3$  sites.

Non-bonded parameters between two different site types (i.e., cross-interactions) are determined using Lorentz-Berthelot combining rules<sup>22</sup> for  $\epsilon$  and  $\sigma$  and an arithmetic mean for the repulsive exponent  $\lambda$  (as recommended in Reference 6):

$$\epsilon_{ij} = \sqrt{\epsilon_{ii}\epsilon_{jj}} \quad (4)$$

$$\sigma_{ij} = \frac{\sigma_{ii} + \sigma_{jj}}{2} \quad (5)$$

Table 3: Non-bonded (intermolecular) parameters for TraPPE,<sup>4,18</sup> MiPPE,<sup>6,20</sup> and NERD.<sup>21</sup>

United-atom	$\epsilon/k_B$ (K)	$\sigma$ (nm)	$\lambda$
TraPPE			
CH <sub>3</sub>	98	0.375	12
CH <sub>2</sub>	46	0.395	12
CH	10	0.468	12
C	0.5	0.640	12
MiPPE			
CH <sub>3</sub>	121.25	0.3783	16
CH <sub>2</sub>	61	0.399	16
CH, gen.	15	0.46	16
C, gen.	1.2	0.61	16
CH, short	15	0.47	16
C, short	1.45	0.61	16
CH, long	14	0.47	16
C, long	1.2	0.62	16
NERD			
CH <sub>3</sub> (not side chain)	104.00	0.3910	12
CH <sub>3</sub> (2-methylpropane)	78.23	0.3880	12
CH <sub>3</sub> (2,2-dimethylpropane)	74.50	0.3910	12
CH <sub>3</sub> (methyl side chain)	70.00	0.3850	12
CH <sub>2</sub>	45.80	0.3930	12
CH	39.70	0.3850	12
C	17.00	0.3910	12

$$\lambda_{ij} = \frac{\lambda_{ii} + \lambda_{jj}}{2} \quad (6)$$

where the  $ij$  subscript refers to cross-interactions and the subscripts  $ii$  and  $jj$  refer to same-site interactions.

## 2.2 Simulation set-up

The majority of results presented in Section 3 are obtained by reprocessing simulation output that were analyzed in previous studies with histogram reweighting.<sup>20,23</sup> New simulation results are provided for 2-methylpropane, 2,2-dimethylpropane, 2,2,4-

trimethylhexane, 2,3-dimethylbutane, 2,3,4-trimethylpentane, 2,2,3,3-tetramethylbutane, and cyclohexane. All simulations are performed using GPU optimized Monte Carlo (GOMC)<sup>24</sup> with Grand Canonical Monte Carlo (GCMC), where the chemical potential ( $\mu$ ), volume ( $V$ ), and temperature ( $T$ ) are constant.

A series of nine simulations are performed, two in the vapor phase, six in the liquid phase, and one near critical which acts as the “bridge” between the vapor and liquid phases. A low-density (less than twenty molecules) initial configuration is utilized for the vapor phase simulations, while the bridge and liquid phase simulations are initialized with a high-density (around 150 molecules) configuration. Initial configurations are generated with Packmol, while psfgen is used to generate the coordinate (\*.pdb) and connectivity (\*.psf) files.

The system volume is the same for each simulation, but varies somewhat between compounds. Specifically, the cubic box side length is 3 nm for all compounds except for 2,3,4-trimethylpentane and 2,2,4-trimethylhexane, which employ a 3.5 nm and 4 nm box length, respectively. The prescribed  $\mu$ ,  $T$ , and  $V$  for the branched alkanes are the same as those utilized in Mick et al.<sup>20</sup> All simulated state points are reported in Supporting Information.

Each GCMC simulation performed in this study consists of an equilibration stage of  $2 \times 10^7$  Monte Carlo steps (MCS). The production stage is  $4 \times 10^7$  MCS for vapor simulations and  $2.5 \times 10^7$  MCS for the liquid and “bridge” simulations. Snapshots (i.e., number of molecules, internal energy, and optionally the xyz coordinates) are stored every 200 MCS to reduce the correlation between sequential configurations. Thus, the number of snapshots ( $K_{\text{snaps}}$ ) is  $2 \times 10^5$  for vapor simulations and  $1.25 \times 10^5$  for liquid and “bridge” simulations.

The type of Monte Carlo move implemented for each step is selected randomly with a 30%, 10%, and 60% probability of performing a displacement, rotation, and particle swap



move, respectively. The move probabilities are slightly different for cyclohexane, namely, 30%, 10%, 40%, and 20% for displacement, rotation, particle swap, and crank-shaft moves, respectively. All simulations utilize coupled-decoupled configurational-bias Monte Carlo (CBMC) to enhance the insertion acceptance rate, with 100 angle trials, 30 dihedral trials, 10 initial site trials, and 4 subsequent site trials. The move probabilities are consistent with those of Mick et al. and Barhaghi et al., while the CBMC dihedral trials and initial site trials differ slightly.

### 2.3 GCMC-MBAR compared with GCMC-HR

Converting the GCMC simulation output into phase coexistence properties requires significant post-processing through reweighting. Histogram reweighting (HR) and, more generally, configuration reweighting is an important tool in many fields of molecular simulation. In fact, it has long since been known that it is possible to estimate properties for state  $j$  by reweighting configurations that were sampled with state  $i$ .<sup>1,25–27</sup> For example, umbrella sampling simulations are often processed using the weighted histogram analysis method (WHAM) to compute free energy differences between states. WHAM (or HR) is essentially an approximation of MBAR and, therefore, MBAR should be favored whenever a histogram-free approach is feasible.<sup>28</sup> In this study, we implement MBAR in Python 2.7 through the *pymbar* package.

Before demonstrating how to compute vapor-liquid coexistence with GCMC-MBAR, we review the traditional GCMC-HR approach. We also discuss the steps of this procedure that are the same for both GCMC-HR and GCMC-MBAR. We refer the interested reader to the literature for derivations and more detailed discussion of the GCMC-HR equations (cf. Reference 1).

### 2.3.1 Histogram reweighting

The ensemble average for a given observable ( $O$ , e.g.,  $U$  and  $\frac{N}{V}$ ) is computed with HR according to

$$\langle O(\mu, \beta) \rangle = \sum_U \sum_N O \times Pr(N, U; \mu, \beta) \quad (7)$$

where  $\langle \dots \rangle$  denotes an ensemble average and  $Pr(N, U; \mu, \beta)$  is the probability of observing  $N$  particles with internal energy  $U$  for a given chemical potential ( $\mu$ ) and inverse temperature ( $\beta \equiv \frac{1}{k_B T}$ , where  $k_B$  is the Boltzmann constant). The double summation is computed numerically where  $U$  and  $N$  are discretized into a 2-dimensional histogram. The probability is obtained with HR from

$$Pr(N, U; \mu, \beta) = \frac{\sum_{i=1}^R Pr_i(N, U) \exp(-\beta U + \beta \mu N)}{\sum_{i=1}^R K_i \exp(-\beta_i U + \beta_i \mu_i N + \hat{f}_i)} \quad (8)$$

where  $Pr_i(N, U)$  is the probability of observing  $N$  particles and  $U$  within the histogram bin width,  $R$  is the number of runs (where the  $i^{\text{th}}$  run corresponds to  $\beta_i$  and  $\mu_i$ ),  $K_i$  is the number of observations (“snapshots”) for run  $i$  (i.e.,  $K_i = \sum_{N,U} Pr_i(N, U)$ ), and  $\hat{f}_i$  is an estimate for the reduced free energy, which is calculated with the relationship

$$\hat{f}(\mu, \beta) = -\ln \sum_U \sum_N \frac{\sum_{i=1}^R Pr_i(N, U) \exp(-\beta U + \beta \mu N)}{\sum_{i=1}^R K_i \exp(-\beta_i U + \beta_i \mu_i N + \hat{f}_i)} \quad (9)$$

where  $\hat{f}_i \equiv \hat{f}(\mu_i, \beta_i)$ . Note that because  $\hat{f}_i$  can also be viewed simply as a constant, the literature typically adopts the notation  $C_i$  (or more specifically,  $-C_i$ ) instead of  $\hat{f}_i$ . For a clear comparison with the MBAR expressions, we prefer  $\hat{f}_i$ .

### 2.3.2 Histogram-free reweighting

Equations 7, 8, and 9 only allow for reweighting simulations at a different  $\beta$  and  $\mu$ . By contrast, MBAR can also be applied to reweight simulations for different force field parameters ( $\theta$ ). The analogous MBAR equation to Equation 7 is

$$\langle O(\theta, \mu, \beta) \rangle = \sum_{n=1}^{K_{\text{snaps}}^{\text{tot}}} O(\mathbf{x}_n, N_n; \theta, \mu, \beta) \times W_n(\theta, \mu, \beta) \quad (10)$$

where  $\mathbf{x}_n, N_n$  are configurations sampled from  $i = 1 \dots R$  simulations at inverse temperature ( $\beta_i$ ), chemical potential ( $\mu_i$ ), and force field parameters ( $\theta_i$ ), and  $K_{\text{snaps}}^{\text{tot}} = \sum_i K_i$  is the total number of snapshots for all  $R$  runs.  $W_n(\theta, \beta, \mu)$  is the weight of the  $n^{\text{th}}$  configuration in a simulation with arbitrary  $\mu, \beta$ , and  $\theta$ .  $W_n$  is computed with the following expression (analogous to Equation 8)

$$W_n(\theta, \beta, \mu) = \frac{\exp[\hat{f}(\theta, \beta, \mu) - u(\mathbf{x}_n, N_n; \theta, \beta, \mu)]}{\sum_{i=1}^R K_i \exp[\hat{f}(\theta_i, \beta_i, \mu_i) - u(\mathbf{x}_n, N_n; \theta_i, \beta_i, \mu_i)]} \quad (11)$$

where  $\hat{f}(\theta, \beta, \mu)$  is the reduced free energy,  $K_i$  are the total number of snapshots from the  $i^{\text{th}}$  run, and  $u(\mathbf{x}_n, N_n; \theta, \beta, \mu)$  is the reduced potential energy evaluated with  $\theta, \beta$ , and  $\mu$  for configuration  $\mathbf{x}_n, N_n$ . The reduced free energy is computed with an expression analogous to Equation 9

$$\hat{f}(\theta, \beta, \mu) = -\ln \sum_{n=1}^{K_{\text{snaps}}^{\text{tot}}} \frac{\exp[-u(\mathbf{x}_n, N_n; \theta, \beta, \mu)]}{\sum_{i=1}^R K_i \exp[\hat{f}(\theta_i, \beta_i, \mu_i) - u(\mathbf{x}_n, N_n; \theta_i, \beta_i, \mu_i)]} \quad (12)$$

For the grand canonical ensemble, the reduced potential energy is

$$u(\mathbf{x}_n, N_n; \theta, \beta, \mu) = \beta U(\mathbf{x}_n, N_n; \theta) - \beta \mu N_n \quad (13)$$

### 2.3.3 Comparison between HR and MBAR

The similarities between MBAR (Equations 11 and 12) and HR (Equations 8 and 9) are readily apparent after substituting Equation 13 into Equations 11 and 12. Indeed, the difference between HR and MBAR is primarily that of bookkeeping, although the histogram-free approach of MBAR does have some benefits when varying force field parameters, as discussed below.

Both HR and MBAR require solving a system of  $R - 1$  nonlinear equations for self-consistency (Equations 8 and 9 for HR and Equations 11 and 12 for MBAR). Specifically, initial guesses for  $C_i$  (HR) or  $\hat{f}$  (MBAR) are updated iteratively until convergence is achieved for the respective equations. There is provably only one solution, so as long as certain criteria are met that will be discussed below. Thus, although a range of different solver methods exist, the only difference is efficiency and numerical stability. MRSHIRTS: I am not sure that we discuss the “certain criteria.” Could you elaborate on this some more?

A key advantage of MBAR over HR is that by changing from a sum over histograms to a sum over snapshots, we are free to perform simulations with other conditions besides  $\mu$  and  $\beta$ . For example, we can carry out simulations at different force field parameters ( $\theta_i$ ). In the histogram context, we cannot easily separate out samples in the same  $U$  histogram that were performed with different force field parameters. Furthermore, as MBAR performs a sum over snapshots, we can reevaluate the configurational energy,  $U(\mathbf{x}_n, N_n; \theta_{\text{rr}})$ , with a range of different “rerun” parameter sets.

The  $\theta$  dependence of Equations 10, 11, and 12 can be removed by performing all  $R$  simulations with a single reference force field ( $\theta_{\text{ref}}$ ) and only computing  $W_n$  and  $\hat{f}$  for  $\theta = \theta_i = \theta_{\text{ref}}$ . With this simplification, these two sets of equations (HR: Equations 7, 8, and 9, MBAR: Equations 10, 11, and 12) can be seen as equivalent in the limit of infinitesimal histogram bin widths. In the zero bin width limit, no histogram contains more than 1

snapshot and, therefore,  $U$  and  $N$  for each histogram can be taken to be the  $U(\mathbf{x}_n, N_n)$  and  $N_n$  of the single observation in that histogram, while histograms with no particles can be omitted. Thus,  $Pr_i(N, U)$  is either 1 or 0, and the sum over all histograms becomes a sum over snapshots conducted in all  $R$  simulation runs. Equations 8 and 9 then reduce to Equations 11 and 12, respectively.

### 2.3.4 Computing saturation properties

For both HR and MBAR, the pressure is computed from

$$P = \frac{k_B T}{V} \ln \Xi + B = \hat{f} + B \quad (14)$$

where  $\Xi$  is the grand partition function and  $B$  is an additive constant. For both HR and MBAR,  $B$  is determined by fitting a straight-line to  $\ln \Xi$  with respect to  $N$  at very low densities. At these low densities, the system is assumed to behave as an ideal gas and, therefore, the slope is unity and  $B = \frac{k_B T}{V} \times b$ , where  $b$  is the y-intercept from the straight-line regression.

The saturated vapor pressure ( $P_{\text{vap}}^{\text{sat}}$ ) is computed with Equation 14 at the desired saturation temperature ( $T^{\text{sat}}$ ) and corresponding saturation chemical potential ( $\mu^{\text{sat}}$ ).  $\mu^{\text{sat}}$  is determined by equating the pressures in the vapor and liquid phases at a fixed value of  $T^{\text{sat}}$ . This is done by integrating  $Pr$  (HR) or  $W_n$  (MBAR) for the two phases separately, i.e., by dividing the snapshots into low and high density regimes. For example, the equality of pressures is satisfied for HR when

$$\sum_U \sum_{N > N_c} Pr(N, U; \mu^{\text{sat}}, \beta^{\text{sat}}) = \sum_U \sum_{N \leq N_c} Pr(N, U; \mu^{\text{sat}}, \beta^{\text{sat}}) \quad (15)$$

where  $N_c$  is an estimate for the number of molecules at the critical density, which serves

to distinguish between snapshots that are in the vapor or liquid phases. The analogous MBAR equation is

$$\sum_{n=1}^{K_{\text{snaps}}^{\text{liq}}} W_n(\theta, \beta, \mu) = \sum_{n=1}^{K_{\text{snaps}}^{\text{vap}}} W_n(\theta, \beta, \mu) \quad (16)$$

where  $N_n$  is the number of molecules in the  $n^{\text{th}}$  snapshot and  $K_{\text{snaps}}^{\text{liq}}$  and  $K_{\text{snaps}}^{\text{vap}}$  are the number of liquid and vapor snapshots, respectively.

By solving Equations 15 (HR) or 16 (MBAR) for  $\mu^{\text{sat}}$ , the vapor and liquid saturation densities and energies ( $\rho_{\text{liq}}^{\text{sat}}$ ,  $\rho_{\text{vap}}^{\text{sat}}$ ,  $U_{\text{liq}}^{\text{sat}}$ , and  $U_{\text{vap}}^{\text{sat}}$ ) are also computed with a modified version of Equations 7 (HR) or 10 (MBAR) where only snapshots from the desired phase are included in the weighted average. For example, when computing  $\rho_{\text{liq}}^{\text{sat}}$  and  $U_{\text{liq}}^{\text{sat}}$ , the double summation in Equation 7 (HR) is performed only for  $N > N_c$  and the sum in Equation 10 (MBAR) is only over  $K_{\text{snaps}}^{\text{liq}}$  liquid snapshots.

Having computed the pressure, internal energies, and densities for the saturated vapor and saturated liquid, the enthalpy of vaporization is calculated with

$$\Delta H_v = \bar{U}_{\text{vap}}^{\text{sat}} - \bar{U}_{\text{liq}}^{\text{sat}} + P_{\text{vap}}^{\text{sat}}(\bar{V}_{\text{vap}}^{\text{sat}} - \bar{V}_{\text{liq}}^{\text{sat}}) \quad (17)$$

where  $\bar{U}$  and  $\bar{V}$  denote molar energy and molar volume, respectively.

### 2.3.5 Number of effective samples

The performance of HR and MBAR depends primarily on good phase space overlap. For HR, good overlap means that the different sets of  $T$  and  $\mu$  sample configurations and densities that are representative of the vapor and liquid phases at  $T^{\text{sat}}$  and  $\mu^{\text{sat}}$ . For MBAR, an additional requirement is that the configurations sampled with  $\theta_{\text{ref}}$  also represent feasible configurations for  $\theta_{\text{tr}}$ .<sup>11,29</sup> The amount of overlap can be quantified by the

number of effective snapshots ( $K_{\text{snaps}}^{\text{eff}}$ ),<sup>30</sup> using Kish’s formula:

$$K_{\text{snaps}}^{\text{eff}} = \frac{(\sum_n W_n)^2}{\sum_n W_n^2} \quad (18)$$

which reduces to  $K_{\text{snaps}}^{\text{eff}} = (\sum_n W_n^2)^{-1}$  when the weights are normalized. This has the property that when the weights are equal,  $K_{\text{snaps}}^{\text{eff}} = K_{\text{snaps}}^{\text{tot}}$ , when all but one weight is negligible,  $K_{\text{snaps}}^{\text{eff}} \approx 1$ , and behaves appropriately for intermediate cases. Messerly et al. proposed a heuristic that MBAR-ITIC is reliable when  $K_{\text{snaps}}^{\text{eff}} > 50$ . We test whether this is a reasonable heuristic for GCMC-MBAR as well.

## 2.4 Basis functions

When applying GCMC-MBAR to different force field parameter sets,  $\theta_{\text{rr}} \neq \theta_{\text{ref}}$ , it is necessary to recompute the internal energy for each snapshot (Equation 13). GCMC-HR typically requires millions of snapshots for precise estimates of  $\rho_{\text{liq}}^{\text{sat}}$ ,  $\rho_{\text{vap}}^{\text{sat}}$ ,  $P_{\text{vap}}^{\text{sat}}$ , and  $\Delta H_v$ . The naive approach when  $\theta_{\text{rr}} \neq \theta_{\text{ref}}$  is to store the molecular configurations ( $\mathbf{x}_n$ ) at each snapshot and then recompute  $U(\mathbf{x}_n, N_n; \theta_{\text{rr}})$ . Although this “rerun” process is orders of magnitude faster than performing direct GCMC simulations with  $\theta_{\text{rr}}$ , the naive approach is memory intensive and computationally expensive. Fortunately, basis functions can greatly accelerate the energy recomputation step.<sup>11,29</sup> We utilize basis functions to rapidly recompute the non-bonded energies when  $\theta_{\text{rr}} \neq \theta_{\text{ref}}$ .

Basis functions are applicable whenever the energy can be separated linearly with respect to the parameters. For example, the Mie  $\lambda$ -6 non-bonded energy is separated into a repulsive and attractive term that can be expressed as

$$u^{\text{nb}}(C_6, C_\lambda; r) = C_\lambda r^{-\lambda} - C_6 r^{-6} \quad (19)$$

where  $C_6$  and  $C_\lambda$  are proportional to  $\epsilon\sigma^6$  and  $\epsilon\sigma^\lambda$ , respectively. Therefore, the total non-bonded energy between all  $\alpha$  and  $\beta$  sites ( $U_{\alpha\beta}^{\text{nb}}$ ) is simply

$$U_{\alpha\beta}^{\text{nb}}(C_6, C_\lambda) = C_\lambda \sum_{i \neq j} r_{ij}^{-\lambda} - C_6 \sum_{i \neq j} r_{ij}^{-6} = C_\lambda \Psi_r + C_6 \Psi_a \quad (20)$$

where  $\Psi_r (\equiv \sum_{i \neq j} r_{ij}^{-\lambda})$  is the repulsive basis function,  $\Psi_a (\equiv \sum_{i \neq j} r_{ij}^{-6})$  is the attractive basis function and, for simplicity,  $\sum_{i \neq j}$  denotes a sum over all unique pairwise interactions.

With Equation 20, the total non-bonded internal energy for all interaction sites of all  $K_{\text{snaps}}^{\text{tot}}$  snapshots can be recomputed for any  $\epsilon$  and  $\sigma$  with linear algebra instead of computing  $u^{\text{nb}}(\theta_{\text{rr}}; r_{ij})$  for each unique pairwise interaction. Because  $C_\lambda$  depends on  $\lambda$ , a separate repulsive basis function is required for each value of  $\lambda$ . Storing  $\Psi_r$  and  $\Psi_a$  for  $K_{\text{snaps}}^{\text{tot}}$  snapshots also greatly reduces the memory storage load compared to storing  $K_{\text{snaps}}^{\text{tot}}$  configurational snapshots (which must be full-precision for reliable “rerun” results).

## 2.5 $\epsilon$ -scaling

Recently, Weidler and Gross proposed an  $\epsilon$ -scaling approach for converting transferable parameters (namely, TAMie) into individualized (compound-specific) parameters (iTAMie).<sup>31</sup> The philosophy for individualized parameters is that some compounds have sufficient reliable experimental data to refine the force field parameters for a specific molecule. However, refitting all non-bonded parameters simultaneously would likely lead to an underspecified optimization. To avoid overfitting, Weidler and Gross optimize a single adjustable parameter ( $\psi$ ) that scales all the  $\epsilon$  values according to

$$\epsilon_{ii}^{\text{ind}} = \psi \times \epsilon_{ii}^{\text{tran}} \quad (21)$$



where  $\epsilon_{ii}^{\text{ind}}$  is the individualized  $\epsilon$  value for united-atom  $ii$ ,  $\epsilon_{ii}^{\text{tran}}$  is the corresponding transferable  $\epsilon$  value, and  $\psi$  is a fixed value for a given compound.

GCMC-MBAR is ideally suited for this “ $\epsilon$ -scaling” approach for at least two reasons. First, MBAR is most reliable when extrapolating in  $\epsilon$  rather than  $\sigma$  and/or  $\lambda$ .<sup>11</sup> Second, the rate-limiting step for GCMC-MBAR is recomputing the configurational energies for a different force field. Furthermore, storing millions of configuration (“snapshots”) is highly memory intensive. While basis functions (see Section 2.4) alleviate the additional computational cost and reduce the memory load,  $\epsilon$ -scaling does not require storing/recomputing configurations or basis functions. Instead, because  $\epsilon_{\text{rr}} = \psi \times \epsilon_{\text{ref}}$  while  $\sigma_{\text{rr}} = \sigma_{\text{ref}}$  and  $\lambda_{\text{rr}} = \lambda_{\text{ref}}$ , recomputing the total non-bonded energy for each snapshot is simply

$$U_{\text{rr}}^{\text{nb,tot}} = \psi \times U_{\text{ref}}^{\text{nb,tot}} \quad (22)$$

where  $U_{\text{rr}}^{\text{nb,tot}}$  and  $U_{\text{ref}}^{\text{nb,tot}}$  are the total non-bonded energy with  $\theta_{\text{rr}}$  and  $\theta_{\text{ref}}$ , respectively.

### 3 Results

Four different applications for MBAR are demonstrated in this study, where slightly different types of simulation output are required. First, we demonstrate how MBAR yields consistent results to those previously reported using histogram reweighting. The standard simulation output is used in this application, namely, a  $2 \times K_{\text{snaps}}^{\text{tot}}$  array containing the number of molecules and the internal energy for all  $K_{\text{snaps}}^{\text{tot}}$  snapshots. Second, we demonstrate how these same data can be used with MBAR to predict VLE properties when performing  $\epsilon$ -scaling. Third, we investigate how well MBAR can predict VLE for force field  $j$  from configurations sampled with force field  $i$ . In this case, a  $3 \times K_{\text{snaps}}^{\text{tot}}$  array is required, where the additional column is the internal energy computed with force

field  $j$ . Fourth, we demonstrate how storing basis functions is a computationally efficient method for predicting VLE for multiple force fields that are unknown at runtime.

In this section, we present results from several different applications of GCMC-MBAR. First, we compute vapor-liquid coexistence properties in the case where the force field parameters do not change, i.e.,  $\theta_{\text{rr}} = \theta_{\text{ref}}$ . Second, we perform a one-dimensional optimization in the  $\epsilon$ -scaling parameter,  $\psi$ . Third, we determine the reliability of GCMC-MBAR when  $\theta_{\text{rr}} \neq \theta_{\text{ref}}$  for different literature force fields. Fourth, we demonstrate how GCMC-MBAR can be applied to obtain new Mie  $\lambda$ -6 parameters for cyclohexane.

### 3.1 $\theta_{\text{rr}} = \theta_{\text{ref}}$

Section 2.3 demonstrated that MBAR and HR are mathematically equivalent in the limit of zero bin width and when  $\theta_{\text{rr}} = \theta_{\text{ref}}$ . Figure 1 provides numerical validation that GCMC-MBAR and GCMC-HR yield indistinguishable vapor-liquid coexistence properties. The evidence for this conclusion is that the median percent deviation is approximately zero and that the largest deviations are within a few percent. The percent deviations shown in Figure 1 are averaged over the 31 branched alkanes studied by Mick et al. and the 11 alkynes studied by Barhaghi et al.

The GCMC-HR values used in Figure 1 were not recomputed in this study but were taken from the literature.<sup>20,23</sup> For a fair comparison between GCMC-HR and GCMC-MBAR, the GCMC-MBAR values were computed using the same raw simulation data as Mick et al. and Barhaghi et al. However, for simplicity, we only reprocess one of the five replicate simulations.

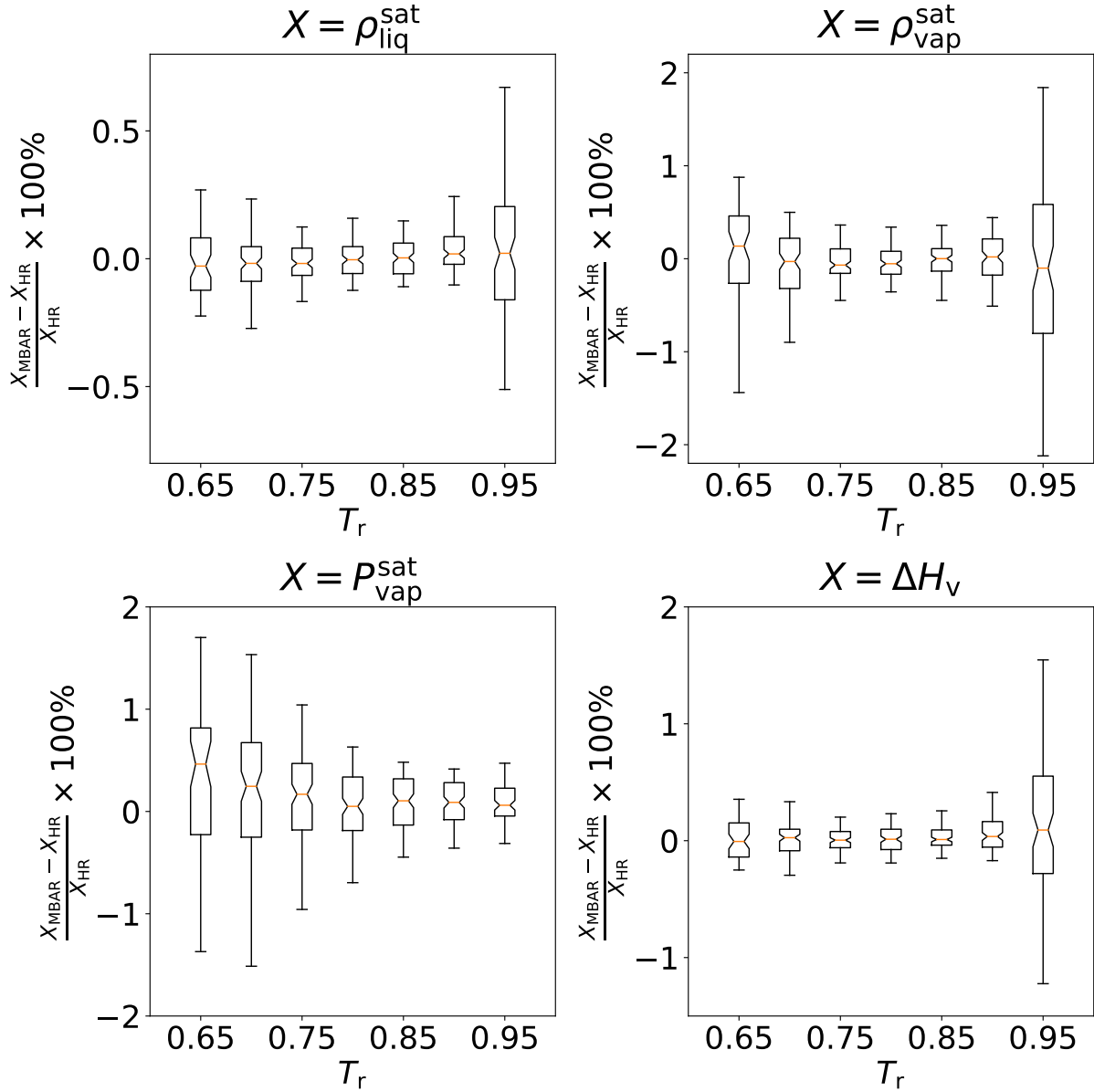


Figure 1: Percent deviations between coexistence properties computed using histogram reweighting (HR) and Multistate Bennett Acceptance Ratio (MBAR). The HR and MBAR results are in good agreement, i.e., within a few percent and an average percent deviation of approximately 0%. Top-left, top-right, bottom-left, and bottom-right panels correspond to saturated liquid density, saturated vapor density, saturated vapor pressure, and enthalpy of vaporization, respectively. Middle line denotes the median deviation, boxes depict the first and third quartiles, and whiskers represent the range that contains 95% of the data.

### 3.2 $\epsilon_{\text{rr}} = \psi \epsilon_{\text{ref}}$

Figure 2 presents the  $\epsilon$ -scaling results for 8 branched alkanes and 11 alkynes using the MiPPE force field as the initial force field. For consistency with the original MiPPE optimization, we use the same scoring function for the branched alkanes and alkynes as Mick et al. and Barhaghi et al., respectively

$$\begin{aligned}
 S = \frac{1}{N_{\text{exp}}} & \left[ w_0 \sum_{j=0}^{N_{\text{exp}}} APD(\rho_{\text{liq}}^{\text{sat}}(T_j^{\text{sat}})) + w_1 \sum_{j=0}^{N_{\text{exp}}} APD(\rho_{\text{vap}}^{\text{sat}}(T_j^{\text{sat}})) \right. \\
 & + w_2 \sum_{j=0}^{N_{\text{exp}}} APD(P_{\text{vap}}^{\text{sat}}(T_j^{\text{sat}})) + w_3 \sum_{j=0}^{N_{\text{exp}}} APD(\Delta H_v(T_j^{\text{sat}})) \\
 & + w_4 \sum_{j=0}^{N_{\text{exp}}} \frac{dAPD(\rho_{\text{liq}}^{\text{sat}}(T_j^{\text{sat}}))}{dT} + w_5 \sum_{j=0}^{N_{\text{exp}}} \frac{dAPD(\rho_{\text{vap}}^{\text{sat}}(T_j^{\text{sat}}))}{dT} \\
 & \left. + w_6 \sum_{j=0}^{N_{\text{exp}}} \frac{dAPD(P_{\text{vap}}^{\text{sat}}(T_j^{\text{sat}}))}{dT} + w_7 \sum_{j=0}^{N_{\text{exp}}} \frac{dAPD(\Delta H_v(T_j^{\text{sat}}))}{dT} \right] \quad (23)
 \end{aligned}$$

where  $S$  is the scoring function,  $N_{\text{exp}}$  is the number of experimental data points,  $w_x$  are the weights for property  $x$ ,  $T_j^{\text{sat}}$  are the saturation temperatures for data point  $j$ , and the absolute percent deviation ( $APD$ ) is defined as

$$APD(X) = \left| \frac{X_{\text{sim}} - X_{\text{exp}}}{X_{\text{exp}}} \right| \times 100\% \quad (24)$$

where  $X_{\text{sim}}$  and  $X_{\text{exp}}$  correspond to the respective simulation and (pseudo-) experimental values for property  $X$  (e.g.,  $\rho_{\text{liq}}^{\text{sat}}$ ). Note that the weights ( $w_x$ ) are different for branched alkanes and alkynes, specifically,  $w_x = (0.6135, 0.0123, 0.2455, 0.0245, 0.0613, 0.0061, 0.0245, 0.0123)$  and  $w_x = (0.757, 0, 0.152, 0, 0.076, 0, 0.015, 0)$  for branched alkanes and alkynes, respectively.

In accordance with the work of Mick et al. and Barhaghi et al., the target values ( $X_{\text{exp}}$ )

are computed with pseudo-experimental correlations. The alkyne correlations are from the Design Institute for Physical Properties (DIPPR) while the branched alkane correlations are from the National Institute of Standards and Technology (NIST) Reference Fluid Properties (REFPROP) database.

Figure 2 shows that the alkynes require a greater degree of scaling than the branched alkanes. Weigler et al. tend to characterize the individualization as being useful when the scaling is greater than 0.4% (i.e.,  $|1 - \psi| > 0.004$ ). With this rationale, 3-methylpentane is the only branched alkane that merits  $\epsilon$ -scaling with the MiPPE-SL force field. Similarly, the TAMie force field also found  $\psi \approx 1$  for all branched alkanes, except 3-methylpentane. Although  $\psi$  values for iTAMie were not reported for alkynes, the largest  $\psi$  value for olefins, ethers, and ketones was  $\approx 1.01$ . A truly transferable force field should have  $\psi \approx 1$  for all compounds. Therefore, the transferability of the MiPPE force field appears to be slightly poorer for 2-pentyne and 2-hexyne, which have an optimized  $\psi > 1.01$ . It is also interesting that only 3 out of 19 compounds require  $\psi < 1$ . Thus, the well-depths appear to be slightly underestimated by the MiPPE force field. By contrast, this trend was not observed in Reference 31 for TAMie.

### 3.3 $\epsilon_{\text{ref}} \neq \epsilon_{\text{rr}}, \sigma_{\text{ref}} \neq \sigma_{\text{rr}}, \text{ and } \lambda_{\text{ref}} \neq \lambda_{\text{rr}}$

A more demanding test of GCMC-MBAR than  $\epsilon$ -scaling is to vary several non-bonded parameters simultaneously, including  $\sigma$  and  $\lambda$ . Because it is not possible to visualize a parameter space of greater than two dimensions, we perform this analysis of GCMC-MBAR using the TraPPE, NERD, MiPPE-gen, and MiPPE-SL force fields. Specifically, we utilize GCMC-MBAR to predict coexistence properties for the NERD and MiPPE-SL force fields using configurations sampled from TraPPE and MiPPE-gen, respectively (see Figure 3). We also use GCMC-MBAR to predict coexistence properties for the TraPPE force field by sampling configurations with MiPPE-gen, and vice versa (see Figure 4).

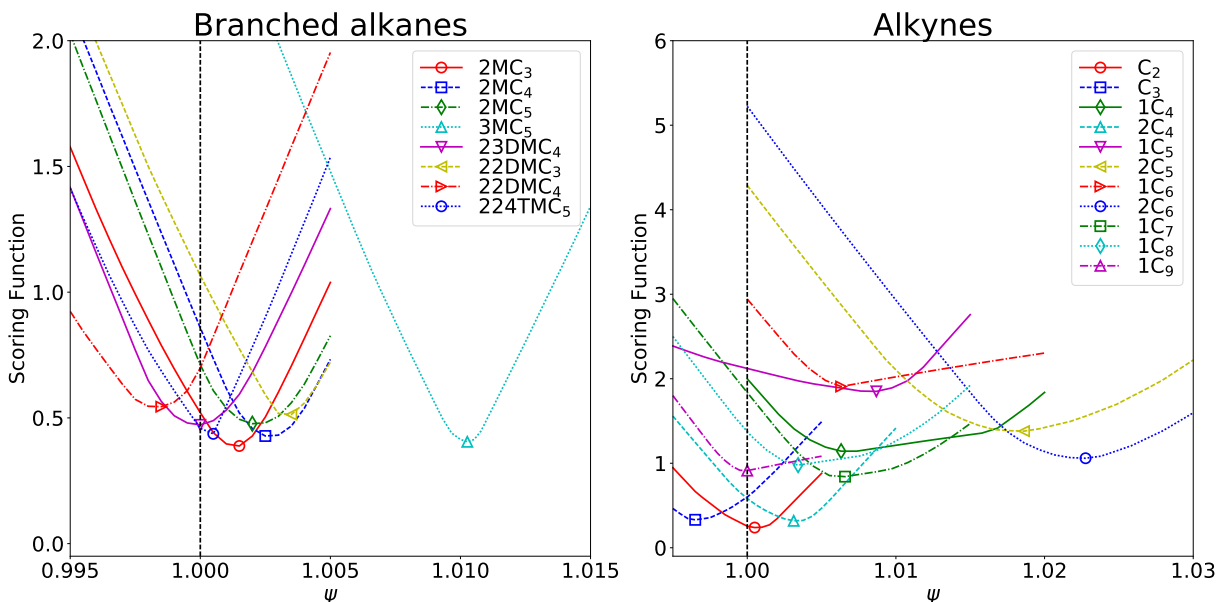


Figure 2: One dimensional optimization with  $\epsilon$ -scaling ( $\psi$ ) of MiPPE-SL for select branched alkanes (left) and alkynes (right). MBAR enables prediction of scoring function over range of  $\psi$  from configurations that were sampled with  $\psi = 1$  (dashed line). Open symbols correspond to the optimal  $\psi$  value for a given compound.

Note that all three non-bonded parameters ( $\epsilon$ ,  $\sigma$ , and  $\lambda$ ) for all four united-atom types (CH<sub>3</sub>, CH<sub>2</sub>, CH, and C) are different between the TraPPE and MiPPE-gen force fields. The TraPPE and NERD  $\epsilon$  and  $\sigma$  values are different for all four united-atom types while  $\lambda = 12$  for both force fields. The MiPPE-gen and MiPPE-SL force fields only differ in the  $\epsilon$  and/or  $\sigma$  values for the CH and C sites. Specifically, the 2-methylpropane and 2,3-dimethylbutane parameters are the same except for  $\sigma_{\text{CH}}$ , the 2,2-dimethylpropane parameters are the same except for  $\epsilon_{\text{C}}$ , the 2,3,4-trimethylpentane parameters are the same except for  $\epsilon_{\text{CH}}$  and  $\sigma_{\text{CH}}$ , and the 2,2,4-trimethylpentane parameters are the same except for  $\epsilon_{\text{CH}}$ ,  $\sigma_{\text{CH}}$ , and  $\sigma_{\text{C}}$ . However, the difference in  $\epsilon$  and  $\sigma$  values for MiPPE-gen and MiPPE-SL is significantly smaller than that between TraPPE and NERD.

Figures 3 and 4 compare the GCMC-MBAR predicted values for  $\theta_{\text{rr}} \neq \theta_{\text{ref}}$  to the literature GCMC-HR values obtained by direct simulation. Figure 3 contains  $\lambda_{\text{rr}} = \lambda_{\text{ref}}$  while Figure 4 corresponds to  $\lambda_{\text{rr}} \neq \lambda_{\text{ref}}$ . As observed in Figures 3 and 4, MBAR is extremely

reliable at predicting vapor phase properties ( $\rho_{\text{vap}}^{\text{sat}}$  and  $P_{\text{vap}}^{\text{sat}}$ ) while it is less reliable for liquid phase properties ( $\rho_{\text{liq}}^{\text{sat}}$  and  $\Delta H_v$ , which depends on both phases). In particular, note that the  $\rho_{\text{liq}}^{\text{sat}}$  estimates in Figure 4 are sporadic and unreliable. This undesirable behavior can be explained by the low number of effective snapshots in the liquid phase.

Figure 5 demonstrates that  $K_{\text{snaps}}^{\text{eff}}$  is typically much greater in the vapor phase than in the liquid phase. Messerly et al. report that MBAR-ITIC is reliable if  $K_{\text{snaps}}^{\text{eff}} > 50$ . Applying this heuristic to GCMC-MBAR helps qualify why the liquid properties are poorly estimated in some systems while the vapor properties are much more accurate. Specifically,  $K_{\text{snaps}}^{\text{eff}}$  is less than 50 in the liquid phase when  $\lambda_{\text{rr}} \neq \lambda_{\text{ref}}$  (TraPPE  $\leftrightarrow$  MiPPE-gen), and is only greater than 50 for  $\theta_{\text{rr}} \approx \theta_{\text{ref}}$  (MiPPE-gen  $\rightarrow$  MiPPE-SL).

The poor overlap when varying  $\lambda$  is consistent with the MBAR-ITIC results.<sup>11</sup> However, GCMC-MBAR provides considerable improvement in predicting  $\rho_{\text{vap}}^{\text{sat}}$  and  $P_{\text{vap}}^{\text{sat}}$  compared to MBAR-ITIC. For this reason, we recommend reducing the  $\rho_{\text{liq}}^{\text{sat}}$  weight ( $w_0$  and  $w_4$ ) in the scoring function (Equation 23) when varying  $\lambda$ . The degree to which the weight is reduced should depend on the number of effective samples ( $K_{\text{snaps}}^{\text{eff}}$ ).

### 3.4 Case Study: Optimizing cyclohexane Mie $\lambda$ -6 parameters

We have demonstrated that GCMC-MBAR is accurate when  $K_{\text{snaps}}^{\text{eff}} \gg 50$ , which is typically the case in the vapor phase and in the liquid phase when  $\lambda_{\text{rr}} = \lambda_{\text{ref}}$ . In this section, we show the power of GCMC-MBAR to rapidly optimize the Mie  $\lambda$ -6 parameters. We have chosen cyclohexane for this case study as this is a compound for which MiPPE does not yet have non-bonded parameters. Also, as cyclohexane consists of a single united-atom site type, it is a convenient molecule for representing the scoring function in 2-dimensions ( $\epsilon_{\text{CH}_2}$  and  $\sigma_{\text{CH}_2}$  for a given value of  $\lambda_{\text{CH}_2}$ ).

## 4 Discussion/Limitations/Future work

Although GCMC-HR is a standard approach for computing vapor-liquid coexistence, HR can also be applied to GEMC simulations (GEMC-HR).<sup>32</sup> Therefore, while the present study presents how MBAR can be applied to GCMC simulations, an analogous GEMC-MBAR approach is worth investigating in future work.

As ITIC is more reliable at near-triple-point conditions, MBAR-ITIC and MBAR-GCMC can be combined to cover most temperatures that span the vapor-liquid coexistence curve.

1. We recommend that future GCMC-VLE studies report the snapshots of  $N$  and  $U$  and/or basis functions to recompute  $U$  as this allows for future force field optimization
2. Improvements are possible with multiple  $\theta$  or simulating a range of  $\mu$  values

## 5 Conclusions

## 6 Acknowledgments

Mostafa and J. Richard Elliott provided valuable insights.

## References

- (1) Panagiotopoulos, A. Z. Monte Carlo methods for phase equilibria of fluids. *Journal of Physics: Condensed Matter* **2000**, *12*, R25.
- (2) Fern, J. T.; Keffer, D. J.; Steele, W. V. Measuring Coexisting Densities from a Two-Phase Molecular Dynamics Simulation by Voronoi Tessellations. *The Journal of Physical Chemistry B* **2007**, *111*, 3469–3475.



- (3) Razavi, S. M.; Messerly, R. A.; Elliott, J. R. Coexistence Calculation Using the Isothermal-Isochoric Integration Method. **2018**, *Pending publication*.
- (4) Martin, M. G.; Siepmann, J. I. Transferable potentials for phase equilibria. 1. United-atom description of n-alkanes. *J. Phys. Chem. B* **1998**, *102*, 2569–2577.
- (5) Hemmen, A.; Gross, J. Transferable Anisotropic United-Atom Force Field Based on the Mie Potential for Phase Equilibrium Calculations: n-Alkanes and n-Olefins. *J. Phys. Chem. B* **2015**, *119*, 11695–11707.
- (6) Potoff, J. J.; Bernard-Brunel, D. A. Mie Potentials for Phase Equilibria Calculations: Applications to Alkanes and Perfluoroalkanes. *J. Phys. Chem. B* **2009**, *113*, 14725–14731.
- (7) Ungerer, P.; Beauvais, C.; Delhommelle, J.; Boutin, A.; Rousseau, B.; Fuchs, A. H. Optimization of the anisotropic united atoms intermolecular potential for n-alkanes. *J. Chem. Phys.* **2000**, *112*, 5499–5510.
- (8) Messerly, R. A.; KnottsIV, T. A.; Wilding, W. V. Uncertainty quantification and propagation of errors of the Lennard-Jones 12-6 parameters for n-alkanes. *J. Chem. Phys.* **2017**, *146*, 194110.
- (9) Chodera, J. D.; Swope, W. C.; Pitera, J. W.; Seok, C.; Dill, K. A. Use of the weighted histogram analysis method for the analysis of simulated and parallel tempering simulations. *J. Chem. Theory Comput.* **2007**, *3*, 26–41.
- (10) Shirts, M. R.; Chodera, J. D. Statistically optimal analysis of samples from multiple equilibrium states. *J. Chem. Phys.* **2008**, *129*, 124105.
- (11) Messerly, R. A.; Razavi, S. M.; Shirts, M. R. Configuration-Sampling-Based Surrogate

- Models for Rapid Parameterization of Non-Bonded Interactions. *Journal of Chemical Theory and Computation* **2018**, *14*, 3144–3162.
- (12) Messerly, R. A.; Shirts, M. R.; Kazakov, A. F. Uncertainty quantification confirms unreliable extrapolation toward high pressures for united-atom Mie  $\lambda$ -6 force field. *The Journal of Chemical Physics* **2018**, *149*, 114109.
- (13) Razavi, S. M. Optimization of a Transferable Shifted Force Field for Interfaces and Inhomogeneous Fluids using Thermodynamic Integration. M.Sc. thesis, The University of Akron, 2016.
- (14) Kiyohara, K.; Spyriouni, T.; Gubbins, K. E.; Panagiotopoulos, A. Z. Thermodynamic scaling Gibbs ensemble Monte Carlo: a new method for determination of phase coexistence properties of fluids. *Molecular Physics* **1996**, *89*, 965–974.
- (15) Errington, J. R.; Panagiotopoulos, A. Z. Phase equilibria of the modified Buckingham exponential-6 potential from Hamiltonian scaling grand canonical Monte Carlo. *The Journal of Chemical Physics* **1998**, *109*, 1093–1100.
- (16) Errington, J. R.; Panagiotopoulos, A. Z. A new intermolecular potential model for the n-alkane homologous series. *J. Phys. Chem. B* **1999**, *103*, 6314–6322.
- (17) Errington, J. R.; Panagiotopoulos, A. Z. New intermolecular potential models for benzene and cyclohexane. *The Journal of Chemical Physics* **1999**, *111*, 9731–9738.
- (18) Martin, M. G.; Siepmann, J. I. Novel Configurational-Bias Monte Carlo Method for Branched Molecules. Transferable Potentials for Phase Equilibria. 2. United-Atom Description of Branched Alkanes. *The Journal of Physical Chemistry B* **1999**, *103*, 4508–4517.

- (19) Shah, M. S.; Siepmann, J. I.; Tsapatsis, M. Transferable potentials for phase equilibria. Improved united-atom description of ethane and ethylene. *AIChE J.* **2017**, *63*, 5098–5110.
- (20) Mick, J. R.; Soroush Barhaghi, M.; Jackman, B.; Schwiebert, L.; Potoff, J. J. Optimized Mie Potentials for Phase Equilibria: Application to Branched Alkanes. *J. Chem. Eng. Data* **2017**, *62*, 1806–1818.
- (21) Nath, S. K.; Escobedo, F. A.; de Pablo, J. J. On the simulation of vapor-liquid equilibria for alkanes. *J. Chem. Phys.* **1998**, *108*, 9905–9911.
- (22) Allen, M. P.; Tildesley, D. J. *Computer simulation of liquids*; Clarendon Press ; Oxford University Press: Oxford England New York, 1987; pp xix, 385 p.
- (23) Barhaghi, M. S.; Mick, J. R.; Potoff, J. J. Optimised Mie potentials for phase equilibria: application to alkynes. *Molecular Physics* **2017**, *115*, 1378–1388.
- (24) GOMC: <http://github.com/GOMC-WSU>.
- (25) McDonald, I. R.; Singer, K. Machine Calculation of Thermodynamic Properties of a Simple Fluid at Supercritical Temperatures. *The Journal of Chemical Physics* **1967**, *47*, 4766–4772.
- (26) Card, D. N.; Valleau, J. P. Monte Carlo Study of the Thermodynamics of Electrolyte Solutions. *The Journal of Chemical Physics* **1970**, *52*, 6232–6240.
- (27) Wood, W. W. Monte Carlo Calculations for Hard Disks in the Isothermal–Isobaric Ensemble. *The Journal of Chemical Physics* **1968**, *48*, 415–434.
- (28) Duarte Ramos Matos, G.; Kyu, D. Y.; Loeffler, H. H.; Chodera, J. D.; Shirts, M. R.; Mobley, D. L. Approaches for Calculating Solvation Free Energies and Enthalpies

Demonstrated with an Update of the FreeSolv Database. *Journal of Chemical & Engineering Data* **2017**, 62, 1559–1569.

- (29) Naden, L. N.; Shirts, M. R. Rapid Computation of Thermodynamic Properties Over Multidimensional Nonbonded Parameter Spaces using Adaptive Multistate Reweighting. *J. Chem. Theory Comput.* **2016**, 12, 1806–1823.
- (30) Dybeck, E. C.; König, G.; Brooks, B. R.; Shirts, M. R. Comparison of Methods To Reweight from Classical Molecular Simulations to QM/MM Potentials. *J. Chem. Theory Comput.* **2016**, 12, 1466–1480.
- (31) Weidler, D.; Gross, J. Individualized force fields for alkanes, olefins, ethers and ketones based on the transferable anisotropic Mie potential. *Fluid Phase Equilibria* **2018**,
- (32) Boulougouris, G. C.; Peristeras, L. D.; Economou, I. G.; Theodorou, D. N. Predicting fluid phase equilibrium via histogram reweighting with Gibbs ensemble Monte Carlo simulations. *The Journal of Supercritical Fluids* **2010**, 55, 503 – 509, 100th year Anniversary of van der Waals’ Nobel Lecture.

## 7 Supporting Information

### 7.1 MBAR VLE estimates

Provide tables of MBAR estimates

### 7.2 Basis functions

1. Validation that basis functions give accurate energies

### 7.3 Raw data

1. Comparison of 2-D histograms for TraPPE and MiPPE. MBAR overlap, possible?

Probably not without rerunning the simulations.

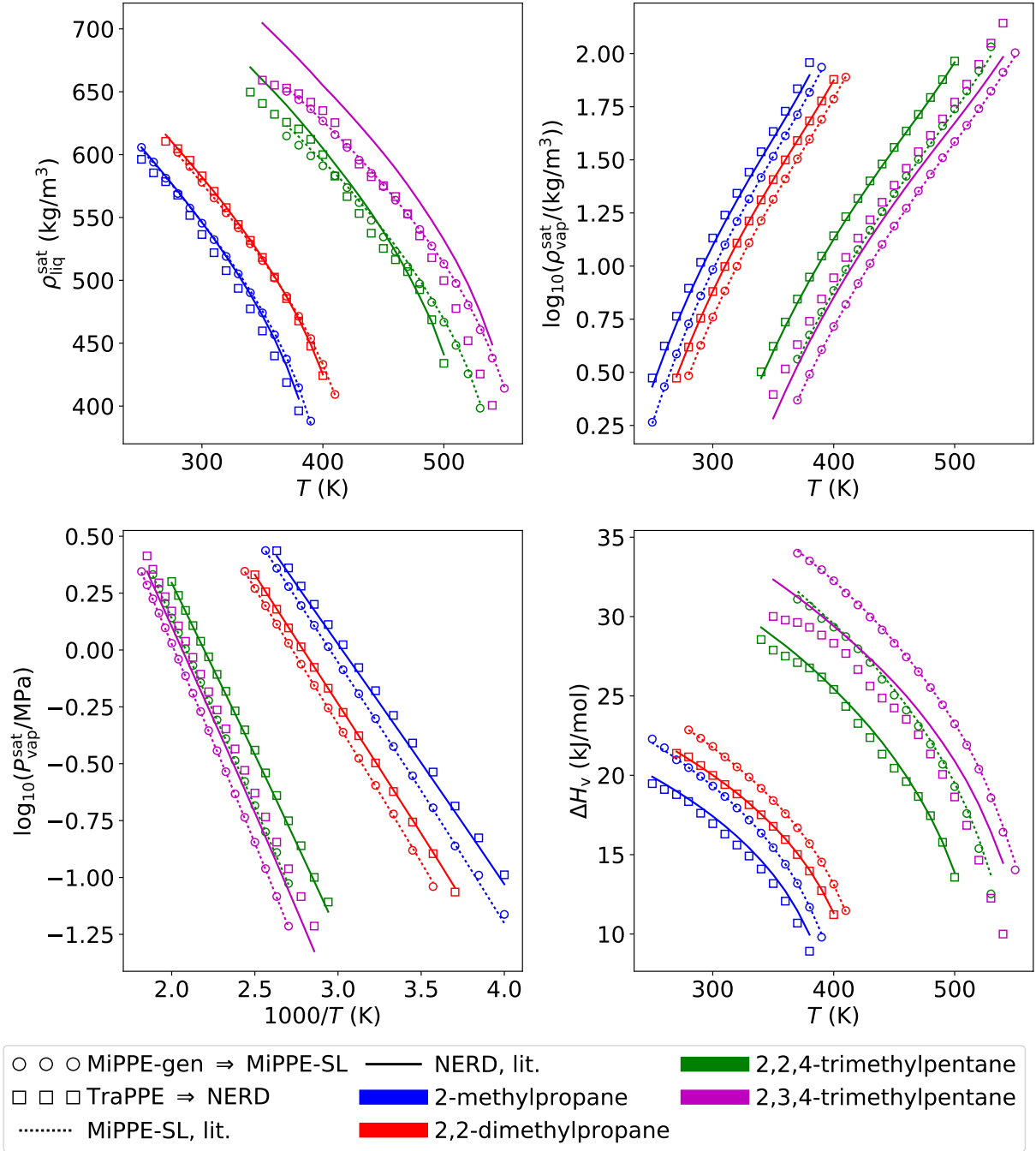


Figure 3: Comparison between MBAR-GCMC estimates (symbols,  $\theta_{\text{rr}} \neq \theta_{\text{ref}}$ ) and MBAR-HR literature values (lines) with a constant repulsive exponent, i.e.,  $\lambda_{\text{rr}} = \lambda_{\text{ref}}$ . MBAR predicts both liquid and vapor properties accurately for  $\lambda_{\text{rr}} = \lambda_{\text{ref}}$ . MBAR-GCMC estimates for the NERD and MiPPE-SL force fields are computed using configurations sampled from TraPPE and MiPPE-gen, respectively. Top-left, top-right, bottom-left, and bottom-right panels correspond to saturated liquid density, saturated vapor density, saturated vapor pressure, and enthalpy of vaporization, respectively.

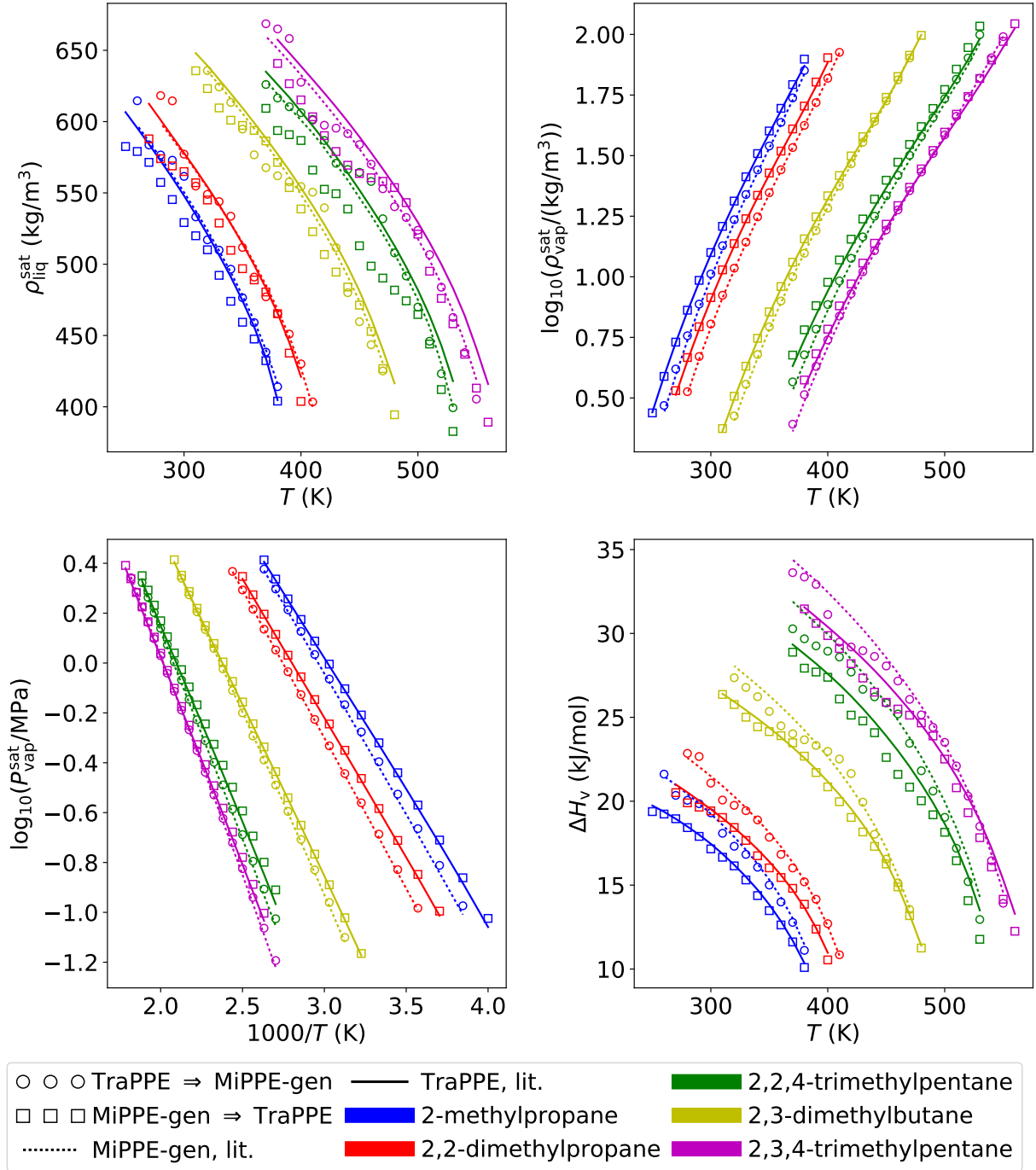


Figure 4: Comparison between MBAR-GCMC estimates (symbols,  $\theta_{rr} \neq \theta_{ref}$ ) and MBAR-HR literature values (lines) with a non-constant repulsive exponent, i.e.,  $\lambda_{rr} \neq \lambda_{ref}$ . MBAR predicts only vapor properties accurately for  $\lambda_{rr} \neq \lambda_{ref}$ . MBAR-GCMC estimates for the TraPPE force field are computed using configurations sampled from MiPPE-gen, and vice versa. Top-left, top-right, bottom-left, and bottom-right panels correspond to saturated liquid density, saturated vapor density, saturated vapor pressure, and enthalpy of vaporization, respectively.

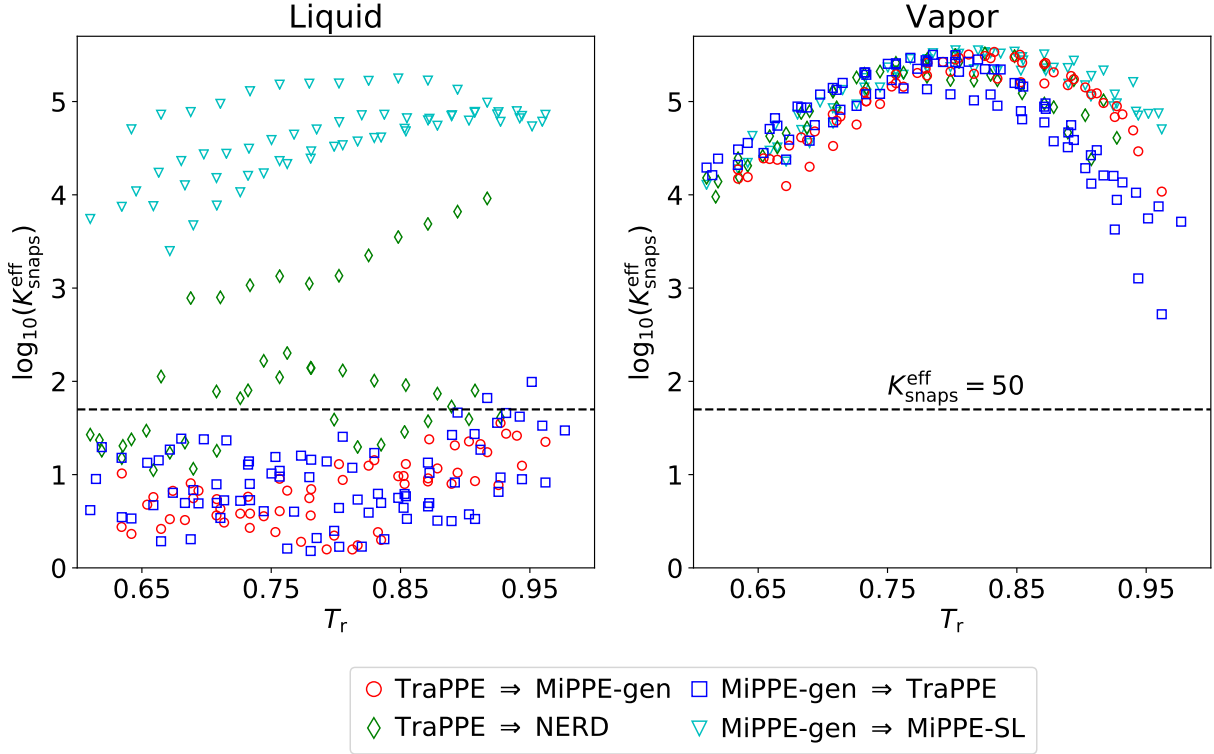


Figure 5: Number of effective snapshots ( $K_{\text{snaps}}^{\text{eff}}$ ) in the liquid (left panel) and vapor (right panel) phases. Good overlap ( $K_{\text{snaps}}^{\text{eff}} \gg 50$ ) is achieved in the vapor phase for each system while poor overlap in liquid phase ( $K_{\text{snaps}}^{\text{eff}} < 50$ ) is observed for  $\lambda_{\text{rr}} \neq \lambda_{\text{ref}}$ . Symbol shapes correspond to Figures 3 and 4. Closed and open symbols correspond to  $\lambda_{\text{rr}} = \lambda_{\text{ref}}$  and  $\lambda_{\text{rr}} \neq \lambda_{\text{ref}}$ , respectively.



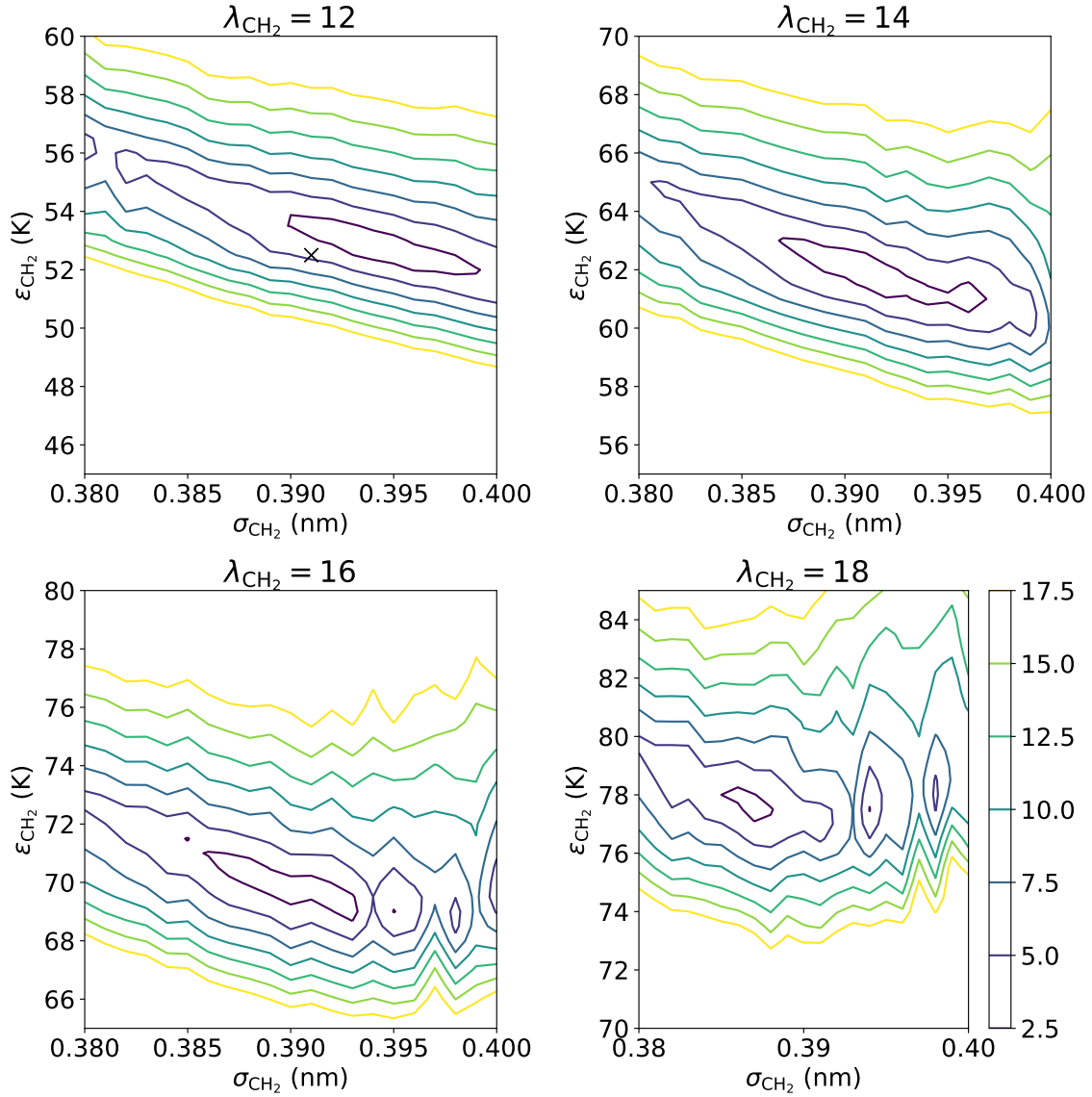


Figure 6: Heat map of scoring function values with respect to  $\epsilon_{\text{CH}_2}$  and  $\sigma_{\text{CH}_2}$  for cyclohexane. GCMC-MBAR enables rapid optimization of Mie  $\lambda$ -6 parameters from a single reference force field ( $\theta_{\text{ref}} = \theta_{\text{TraPPE}}$ ). Top-left, top-right, bottom-left, and bottom-right panels correspond  $\lambda_{\text{CH}_2} = 12$ ,  $\lambda_{\text{CH}_2} = 14$ ,  $\lambda_{\text{CH}_2} = 16$ ,  $\lambda_{\text{CH}_2} = 18$ , respectively. Red region represents the optimal parameter set, i.e., the lowest value of  $S$ .

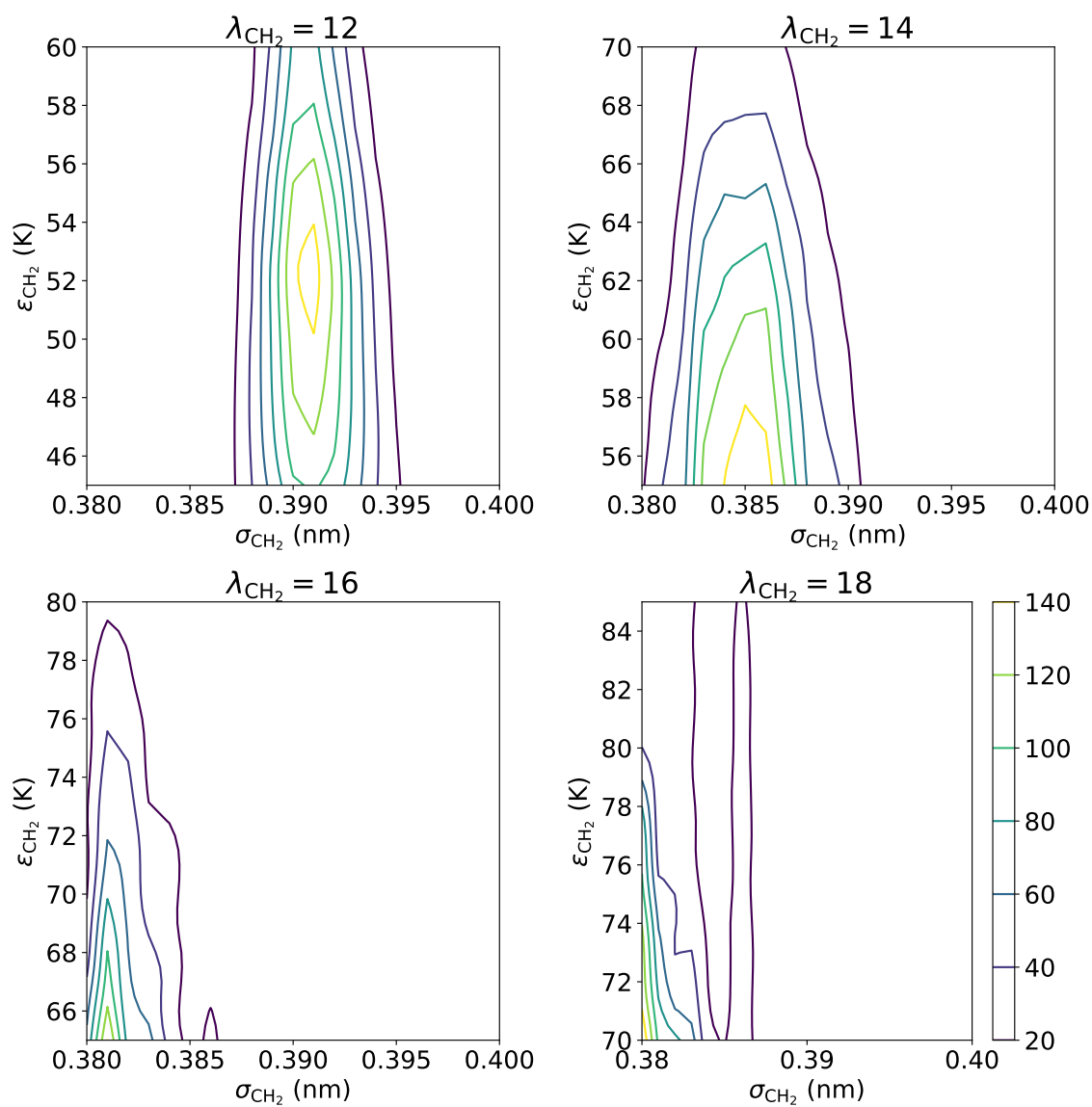


Figure 7